

Push–Pull Electronic Effect and D-Band Center Bi-Modulated Bio-Heterojunction Enzyme Enables All-Stage Infected Wound Healing

Miaomiao He, Qiancun Wang, Zhijie Lin, Dan Sun, Guangfu Yin, Yi Deng,*
and Weizhong Yang*

Pathogenic infections pose a persistent threat to global public health, necessitating innovative antibacterial strategies with well-defined disinfection pathway. The antibacterial efficiency is confined in the contradiction between reactants adsorption and intermediates desorption. Here, the FeMoS₄/MXene bio-heterojunction enzyme (FM BioHJzyme) is proposed and constructed. Under the inspiration of near-infrared light (NIR), the heterostructures between the FeMoS₄ and MXene facilitates efficient electron-hole separation with localized electron accumulation at FeMoS₄ sites. Crucially, the electronic push-pull effect induced by Mo polarizes oxygen-containing reactants (H₂O₂, H₂O, O₂) toward Fe active centers, enabling sequential electron capture for reactive oxygen species (ROS) generation. The results also reveal an enhancement in electron density at Fe sites compared to FeS/MXene controls, which is accompanied by a downshift in the Fe d-band center that reduces intermediates adsorption energy. The therapeutic efficacy is systematically evaluated using an *S. aureus*-infected full-thickness skin defect model. The bi-modulated FM BioHJzyme exhibits favorable antibacterial efficiency under NIR irradiation, while subsequent wound healing is facilitated through collagen deposition and angiogenesis in the following absence of NIR irradiation. This work offers a deep insight into the intricate mechanism-performance relationship of BioHJzyme platform in catalytic anti-bacterial application and proposes a sustainable approach of mechanism-guided materials design.

1. Introduction

The escalating challenge of pathogenic infections has become a critical global public health concern. Once, the discovery of

antibiotics such as penicillin heralded an era of permanent cure in eradicating bacterial infections.^[1] Unfortunately, the evolutionary adaptability of bacteria has led to generate the more robust strains with multidrug resistance.^[2] This alarming trend underscores the imperative to develop next-generation antimicrobial agents. Recent advancements in biotechnology have yielded diverse valuable concepts for the construction of antibacterial and anti-biofilm platforms, which primarily fall into four categories: i) intrinsically bactericidal biomaterials (e.g., antimicrobial peptides,^[3] quaternary ammonium salts,^[4] silver nanoparticles,^[5] zinc oxide,^[6] etc.); ii) photothermal/sonothermal agents^[7]; iii) photocatalytic/sonocatalytic materials generating reactive oxygen species (ROS),^[8] a kind of catalytical antibacterial therapy (CAT); iv) multimodal synergistic therapies.^[9] The researches have noted the antibacterial mechanisms involved physical direct interaction of extremely sharp edges of nanomaterials with cell wall membrane,^[10] ROS generation even in dark,^[11] trapping the cells within the aggregated nanomaterials,^[12] oxidative stress,^[13]

DNA damaging,^[14] and so on. Despite moderate disinfection efficacy, these approaches suffer from intrinsic limitations including narrow-spectrum antimicrobial performance, component-specific bactericidal mechanisms, suboptimal efficiency, and compromised physiological stability.^[15] Notably, ion-release-dependent bactericidal systems further face challenges in sustaining long-term antimicrobial activity.^[16] Consequently, there exists an urgent need for innovative strategies to address the shortcomings of conventional antibacterial therapies and clarify the in-built mechanism for guiding the materials preparation.

In the recent advancements of biotechnology, various materials exhibit favorable effect on the catalytical antibacterial therapy (CAT), distinguished by its high efficiency. Materials like metal-based materials (Ag, ZnO, and Au, etc.), metal-organic frameworks (MOFs) functioned through metal nodes or organic ligands in the structure, and single-atom catalysis characterized by tunable active sites provides ample research perspective.^[17] Moreover, these studies verify the critical role

M. He, Q. Wang, Z. Lin, G. Yin, Y. Deng, W. Yang
College of Biomedical Engineering
School of Chemical Engineering
Sichuan University
Chengdu 610065, China
E-mail: dengyibandeng@scu.edu.cn; ywz@scu.edu.cn

D. Sun
Department Advanced Composite Research Group (ACRG)
School of Mechanical and Aerospace Engineering
Queen's University Belfast
Belfast BT9 5AH, UK

 The ORCID identification number(s) for the author(s) of this article can be found under <https://doi.org/10.1002/adma.202510161>

DOI: 10.1002/adma.202510161

of polyatomic efficiency and interfacial structure modulation in enhancing catalytic performance. Bio-Heterojunction (BioHJ) with abundant heterostructure, comprising two semiconductors with distinct energy levels and bandgaps, enables tailored structural designs, efficient electron-hole separation, and controlled ion release. Our prior work had demonstrated that BioHJs exhibited synergistic photothermal effects and light-triggered ROS generation (“1 + 1 > 2” effect), attributable to energy band/gap modulation.^[18] These heterostructures also display enzyme-mimetic activities (glutathione peroxidase (GPx), peroxidase (POD), catalase (CAT)), which have been nominated as Bio-heterojunction enzyme (BioHJzyme).^[19] Subsequent investigations revealed that heterostructure-induced d-band center shifts critically regulate ROS generation by modulating intermediate desorption.^[20] While upshifted d-band centers enhance the adsorption, downshifted centers favor desorption—a dichotomy underscoring the need for mechanistic insights into adsorption-desorption equilibria to guide materials design.

Building upon these findings, we engineered a bimetal sulfide aggregates (FeMoS₄)/MXene BioHJzyme (FM BioHJzyme) as illustrated in **Scheme 1**. The results revealed that added Mo induces electron redistribution via a push-pull effect comparing with FeS/MXene, polarizing adjacent reactants (H₂O₂, H₂O, and O₂) toward Fe active sites. Notably, Mo incorporation downshifted the Fe d-band center by 1.6 eV, reducing intermediate adsorption energy and thereby enhancing ROS generation. The material mechanism combining push-pull effect and downshifted d-band center exhibited favorable effect on solving the above-mentioned dichotomy. In vitro antibacterial assays demonstrated that the FM group with NIR irradiation can eradicate bacteria with anti-bacterial rate of 99.99% against both *Escherichia coli* (*E. coli*) and *Staphylococcus aureus* (*S. aureus*) mainly by Carbohydrate metabolism pathway. In vivo infected wound healing on rats revealed the bactericidal effect, while the FM accelerated wound healing (88.66% wound closure at day 7 vs. 53.51% in controls) through ECM-receptor interaction, TNF signaling pathway, and biosynthesis of arginine pathways, resulting in the promoted anti-inflammation and collagen deposition. The FM can be prepared as wound dressing, which maintains the superior property in infected wound healing, indicating the various forms of application. This work advances the intricate mechanism-performance relationship of BioHJzyme systems in the catalytic antibacterial application and proposes a sustainable approach of mechanism-guided materials design.

2. Results and Discussion

2.1. Characterization of Samples

The single-layer MXene was prepared by ultrasonic stripping method. FeMoS₄/MXene (FM) BioHJzyme was fabricated through hydrothermal method. As shown in **Figure 1A**, the scanning electron microscope (SEM) images displayed that single-layered MXene nanosheets were prepared, while the FeMoS₄ demonstrated a nanoparticles morphology. For the FM, the FeMoS₄ was in situ grown on the MXene. The morphology detected by the transmission electron microscope (TEM) further verified the successful fabrication of FM, while the high-resolution TEM (HRTEM) manifested the crossing section of the

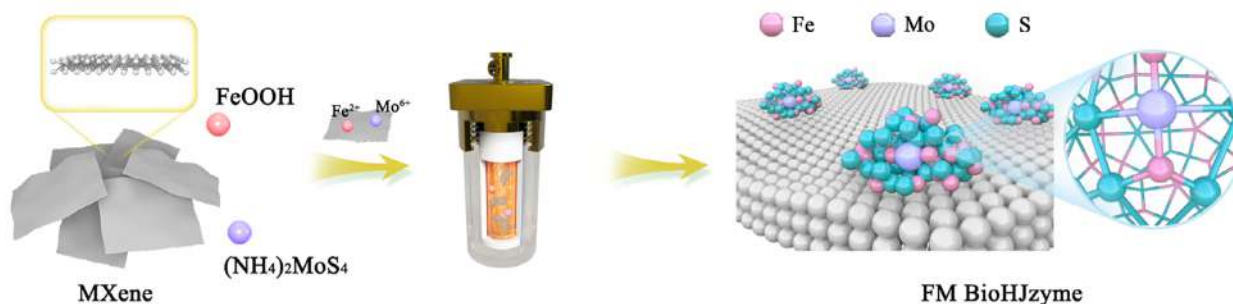
two phases. The interplanar spacing of the MXene was gauged to ≈3.50 Å in line with d-spacing of (002) plane of TiC. The interplanar spacing of FeMoS₄ was ≈1.58 Å in accordance with d-spacing of (110). TEM mapping images demonstrated that the elements consisted by Ti, Fe, Mo, and S. The selected area electron diffraction (SAED) image of FM also indicated the successful integration of the two phases. The characteristic plane (002) and (110) can be found. Moreover, the X-rays diffraction spectra (XRD) of FM (**Figure 1B**) displayed the characteristic peaks of both MXene and FeMoS₄. All the above results demonstrated the successful fabrication of FM. Additionally, Zeta potentials (**Figure 1C**) of FeMoS₄, MXene, FM, and Fe³⁺ + MXene were −26.03, −21.05, −23.57, and −17.34 eV, respectively, which suggested the Fe³⁺ adsorbed on the surface of MXene by electrostatic interaction and became the reaction sites to form FeMoS₄.^[18b]

As shown in **Figure 1D**, the full X-ray photoelectron spectroscopy (XPS) analysis showed that the characteristic elements of FM were Fe, O, Ti, C, Mo, and S, which were the same with EDS mapping results. The deconvolution of Fe 2p, Ti 2p, and Mo 3d in XPS analysis were analyzed (**Figure 1E**). The XPS spectra of Fe 2p appeared that the characteristic peaks at 725.1 and 707.3 eV can be attributed to the Fe (II), while the peak at 711.6 eV can be assigned to Fe (III), indicating the two valence states of Fe.^[18a] Regarding to the Ti 2p, the binding energy at 464.5 and 459.2 eV were corresponded to Ti-O, while the binding energy at 464.6 and 455.7 eV belonged to the Ti-C.^[21] The Mo 3d can be assigned in 3d_{3/2} and 3d_{5/2}. Inductively coupled plasma optical emission spectrometer (ICP-OES) was used to detect the released ions of Fe and Mo (**Figure 1F**). It can be found that the released ions possessed an increased trend with the soak time. Ultraviolet-visible diffuse reflectance spectroscopy (UV-vis-DRS) as shown in **Figure 1G** revealed the FM had full wavelength absorption, therefore, FM can absorb the 808 nm light, which possessed potential NIR-induced capabilities.^[22] The transient photocurrent responses and surface photovoltaic technique (**Figure 1H**) show FM had the higher photocurrent intensity and the stronger photovoltage comparing with FeMoS₄, indicating that FM enhanced the electron-hole separation efficiency owing to the formed heterostructure, which may be conducive to the prominent NIR-activatable ability.

Based on the above characterization of samples structure, the NIR-induced capabilities were subsequently processed. First, the photothermal property was conducted as shown in **Figures 2A** and **S2** (Supporting Information). The photothermal curves of FM with different mass ratio of FeMoS₄ and MXene (1:2, 1:1, and 2:1) exhibited plateau temperature of 55, 50, and 40 °C, respectively, thus, the ratio of 1:1 was chosen for subsequent experiments. The plateau temperature of MXene, FeMoS₄, and FM can reach 55, 37, and 50 °C, respectively, indicating the favorable photothermal performance. The temperature of FM (500 µg mL^{−1}, 1 mL) remained stable over three cycles, which unveiled the superior photothermal stability. The thermal images detected by infrared thermography of samples with different NIR power densities inferred the similar results, while the plateau temperature increased with the improved power density.

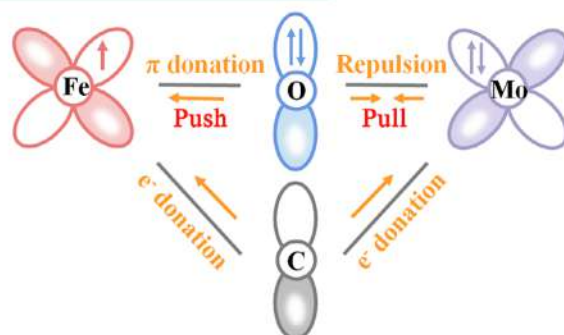
Reactive oxygen species (ROS), including hydroxyl radical (•OH), singlet oxygen (¹O₂), and superoxide radical (•O₂[−]), etc., is a vital participator of antibacterial therapy. Followed, methylene blue (MB), tetramethylbenzidine (TMB), and rhodamine (RhB)

Material Fabrication

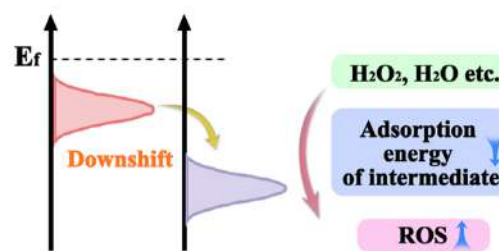


Material Mechanism

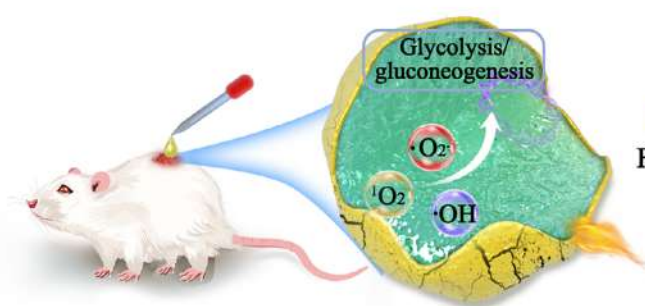
a. Electronic push-pull to enhance the reaction of reactants



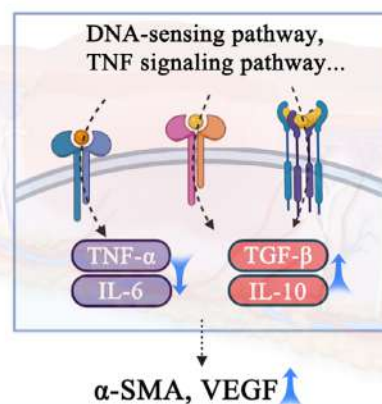
b. Downshifted d-band center decreases the adsorption energy of intermediate



Infected Wound Healing



Following



a. Antibacterial mechanism on Metabolism

b. Anti-inflammatory mechanism for further collagen deposition and angiogenesis

Scheme 1. Schematic illustration of the preparation and functionality of FM BioHJzyme. (In the part of Materials Mechanism, the O from the H₂O₂, O₂, H₂O; the C from MXene; the Fe and Mo from FeMoS₄).

were used to detect •OH, verifying the POD-mimetic activity. As Figure 2B showed, the absorbance had no obvious change for FM group in the absence of NIR irradiation, while the decreased absorbance can be found with NIR irradiation. Furthermore, an increased absorbance tendency can be found for the TMB

experiment with a darker color (Figure 2C). The RhB also exhibited an attenuated tendency as the same to the MB results (Figure 2D). The above results verified that the FM facilitated NIR-induced POD-mimetic activity to produce •OH. Apart from •OH production, 1,3-diphenylisobenzofuran (DPBF) assay

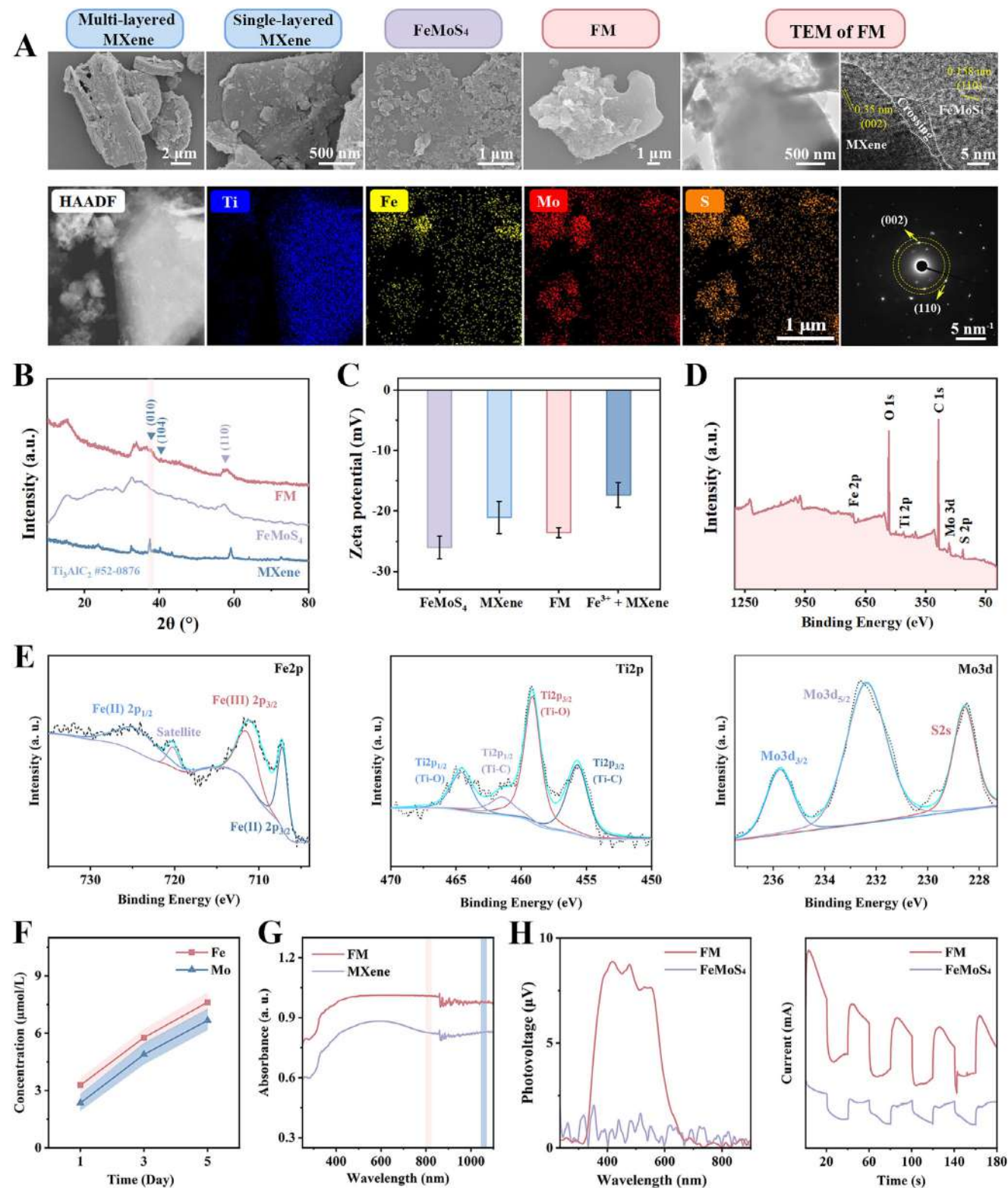


Figure 1. Preliminary characterization of samples. A) SEM images of different samples as well as TEM, HRTEM, HAADF, elemental mapping, and SAED of FM; B) XRD spectra of samples; C) Zeta potentials; D) Full XPS spectra of FM; E) The deconvolution of Fe 2p, Ti 2p and Mo 3d in XPS analysis of FM; F) The released Fe and Mo elements of FM at different time detected by ICP-OES; G) The spectra of UV-vis-DRS; H) The photovoltage and photocurrent of FeMoS₄ and FM.

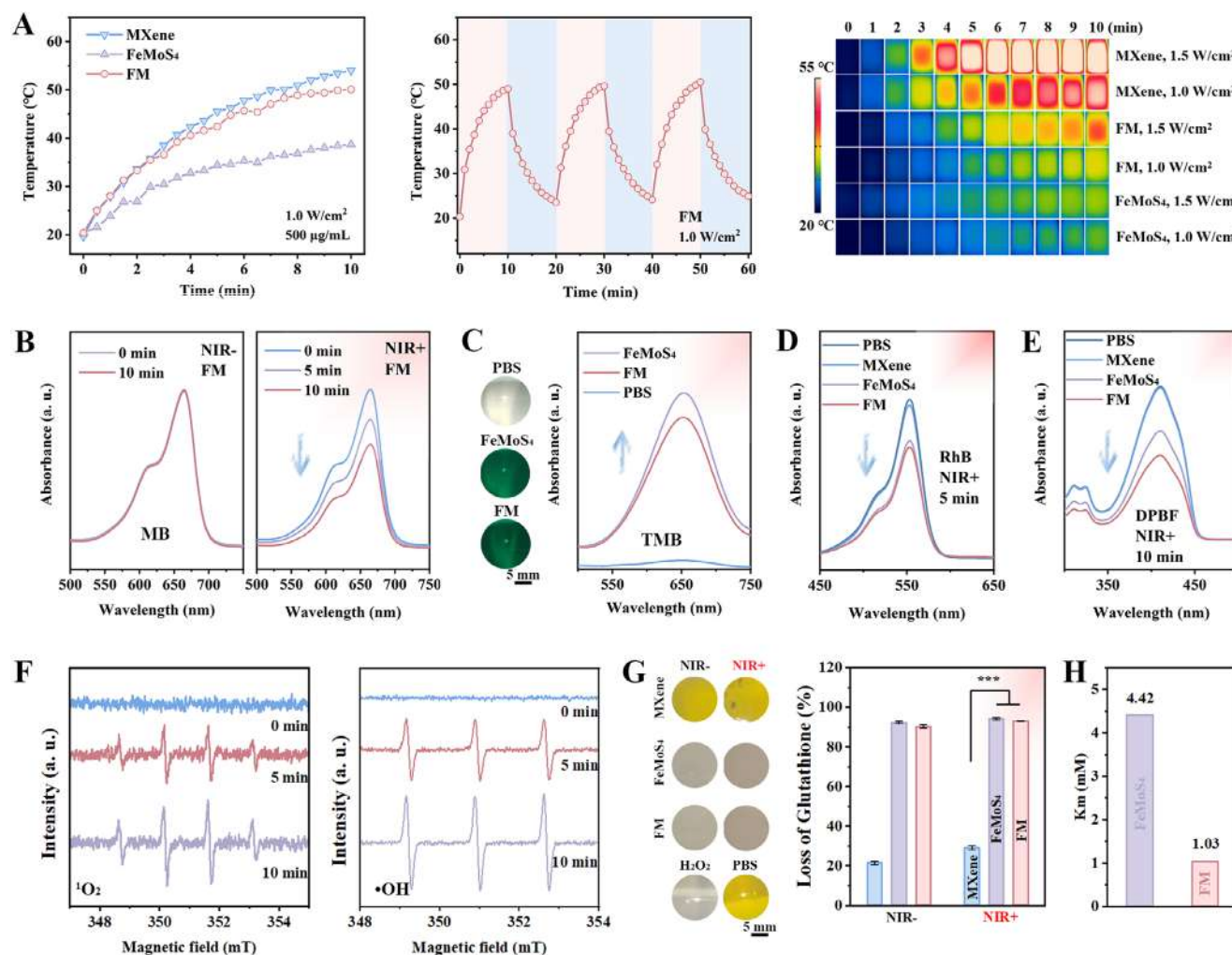


Figure 2. A) Photothermal curves of different samples, photothermal cycle curves of FM, and photothermal images of different samples with different NIR power densities; B) The MB absorbance spectra of FM group with/without NIR irradiation for detecting •OH; C) The TMB absorbance spectra of different samples and its photos for detecting •OH; D) The RhB spectra of samples with NIR irradiation for detecting •OH; E) The DPBF spectra of samples with NIR irradiation for detecting ¹O₂/•O₂⁻; F) ESR spectra of FM for ¹O₂ and •OH; G) The recorded pictures and its quantitative analysis of GSH consumption; H) Km value of FeMoS₄ and FM detected by TMB. (*n* = 5; **p* < 0.05, ***p* < 0.01, ****p* < 0.001).

was processed for detecting O₂ related ROS (¹O₂/•O₂⁻), which stemmed from the reaction between DPBF and ¹O₂/•O₂⁻ and convert DPBF into colorless 1,2-dibenzoylbenzene.^[23] As shown in Figure 2E, under NIR irradiation, the comparatively lower absorbance intensity can be found in FM group, indicating the stronger capability to produce ¹O₂/•O₂⁻. Electron spin resonance (ESR) was applied to confirm the species of ROS. As displayed in Figure 2F, the representative 1:1:1 ¹O₂ signals and 1:2:2:1 •OH signals are amplified dramatically with NIR irradiation, suggesting the species identification of ¹O₂ and •OH.

Glutathione (GSH), a major endogenous antioxidant secreted by bacteria, can be oxidized to glutathione disulfide (GSSG) under oxidative stress to protect bacteria from ROS injury.^[24] There, the GPx-mimetic activity presenting the GSH consumption ability was detected by 5,5'-dithiol-bis-(2-nitrobenzoic acid) (DTNB).^[25] Figure 2G showed the photos of color change and its quantitative analysis in different group, both the FeMoS₄ and FM groups consumed GSH, which were even further

enhanced with NIR irradiation, resulting in a NIR-enhanced GPx-mimetic activity. Additionally, the TMB was also used in testing the Michaelis constant (Km), reflecting the catalytic efficiency to produce •OH. The smaller Km value, the higher catalytic efficiency.^[26] As Figure 2H showed, the Km of FM was lower than FeMoS₄, indicating the improved catalytic efficiency of FM, which is originated from the special heterostructure between the phases of MXene and FeMoS₄.

Owing to the favorable NIR-induced and NIR-enhanced capabilities, the intrinsic mechanisms of materials structure were systematically investigated through density functional theory (DFT) calculations. Figure 3A showed that the work functions of MXene, FeMoS₄, and FM were 5.79, 4.25, and 4.06 eV, respectively. The smaller work function of FM indicated enhanced electron transport, which facilitated electron-hole separation and underpins its above-mentioned NIR-induced/enhanced capabilities. Differential charge density (Figure 3B) of FM revealed significant electron accumulation in FeMoS₄ and electron depletion

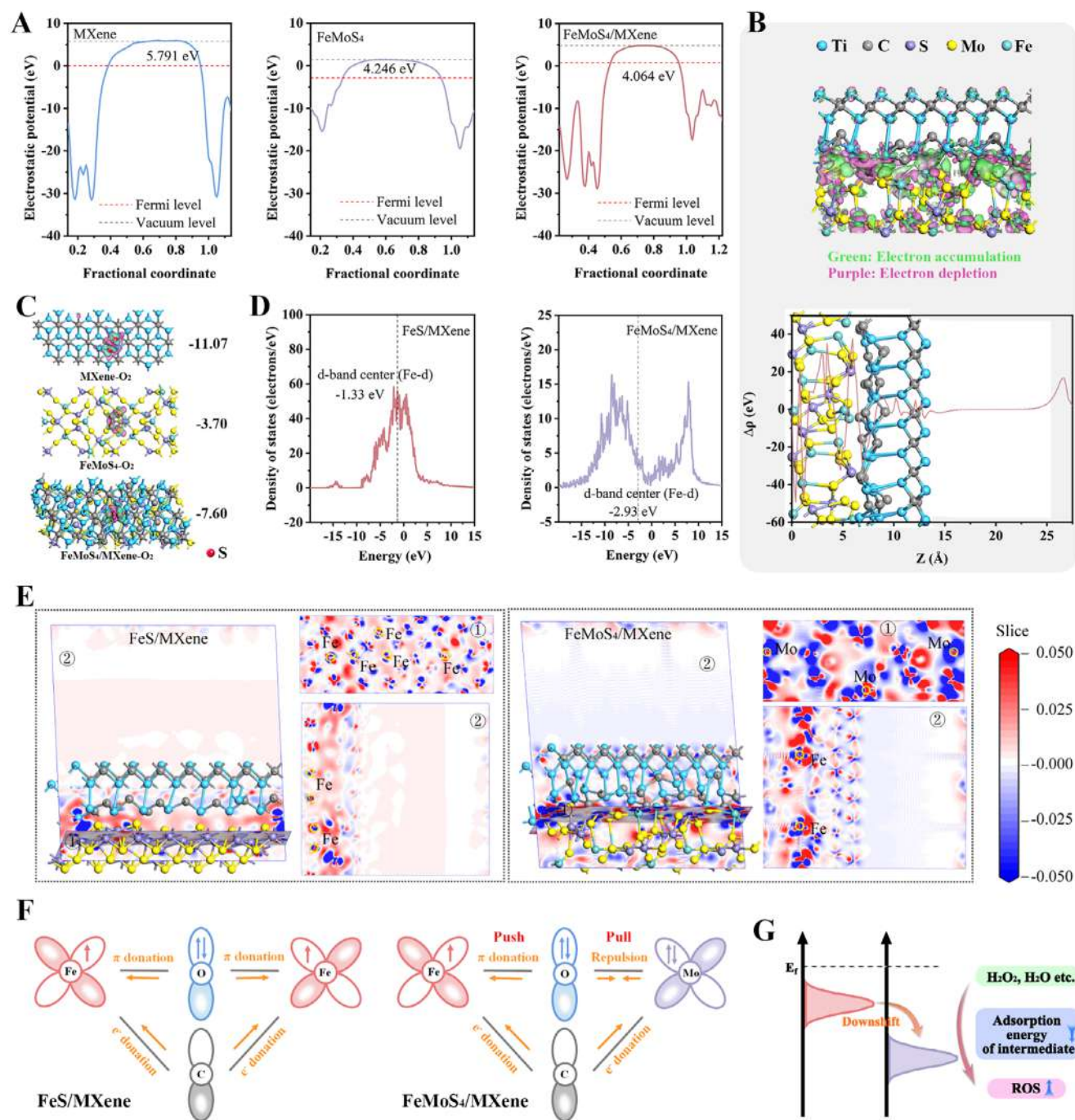


Figure 3. DFT Calculation. A) Work function of samples; B) The differential charge-density map for the direction of electron transfer; C) O_2 adsorption energy of samples; D) The energy of d-band center of $\text{FeMoS}_4/\text{MXene}$ in comparison with FeS/MXene ; E) Calculated 3D charge density differences and the top/side planes for three models. The red and blue isosurface refer to the electron accumulation and electron depletion, respectively; F) Schematic illustration of the push–pull electronic effects owing to the produced Mo; G) Schematic illustration of the downshifted d-band center of Fe.

localized on MXene, confirming unidirectional electron transfer from MXene to FeMoS_4 , where MXene acted as an electron donor. The O_2 adsorption energies of MXene, FeMoS_4 , and FM were -11.07 , -3.70 and -7.60 eV, respectively (Figure 3C). The more negative adsorption energy correlates with stronger adsorption capacity. The purple region was mainly located in the center

of three adjacent Ti, indicating that the electron transfer direction was from MXene to O when FM contacted with adjacent reactants, such as O_2 . To elucidate the impact of Mo, the d-band center of Fe atoms in FM was compared with that of the FeS/MXene control group. As shown in Figure 3D, the d-band center shifted from -1.33 eV in FeS/MXene to -2.93 eV in FM, indicating that

Mo incorporation effectively lowered the d-band center of Fe. This observation aligns with prior studies linking d-band center position to catalyst-adsorbate interaction strength.^[20]

Crucially, comparative differential charge density analyses (top and side views, Figure 3E) between FeS/MXene and FM revealed the expanded electron accumulation/depletion zones in FM, validating enhanced electron-hole separation driven by the Mo-induced push-pull electronic effect. The proposed mechanism is schematically summarized in Figure 3F,G. In terms of FeS/MXene, Fe cations interact with bridging O via π -donation.^[27] Upon Mo incorporation, the electron repulsion between Mo cations and O strengthens the π -donation between Fe cations and O, enabling partial electron transfer from Mo to Fe.^[28] The push-pull electronic effect promotes electron redistribution endows the reactants adopt more electron to produce ROS.^[29] Concurrently, electron-rich MXene as one of the components, mitigates electron deficiency through charge donation.^[30] Mo optimizes the d-orbital configuration of Fe, inducing a pronounced downward shift in the d-band center. This shift corresponds to increased occupancy of antibonding states, thereby weakening intermediate adsorption and improving catalytic efficiency.^[31]

Building on the favorable NIR-induced and NIR-enhanced properties, as well as the elucidated structure-dependent mechanisms, the in vitro antibacterial performance of the samples was systematically evaluated under both NIR-irradiated and non-irradiated conditions. The antibacterial ability of FM at different concentrations and NIR irradiation times has been detected as shown in Figures S6 and S7 (Supporting Information). The results indicate that the concentration of 0.2 mg L⁻¹ and 10 min NIR irradiation time are suitable parameters. Figure 4A showed the Live/Dead staining, SEM images, and florescent ROS stained by DCFH-DA of *E. coli* and *S. aureus*, respectively. In the absence of NIR irradiation, the proportion of dead bacteria (red) followed the trend: FM > FeMoS₄ > MXene > PBS. Remarkably, NIR irradiation boosted FM's bactericidal efficiency to 99.99% against both *E. coli* and *S. aureus*. From the bacterial SEM images, an obvious bacterial surface wrinkling and breakage can be found in the groups of FeMoS₄ + NIR and FM + NIR. ROS levels within the bacteria were also detected. The optimum ROS intensity can be found in the FM + NIR group. The corresponding quantitative analysis was also displayed in Figure 4B. The bacterial ROS intensities were significantly improved under NIR irradiation. Figure 4C,D shows the spread plate photographs and the corresponding antibacterial efficiency against *S. aureus* and *E. coli*, respectively. The bacterial colonies in FM + NIR are significantly decreased, indicating most of the bacteria are dead. The corresponding antibacterial rate against *E. coli* and *S. aureus* were 99.99% and 99.99%, respectively. The bacterial TEM images of FM group with/without NIR irradiation were captured as shown in Figure 4E. The markedly deformed shape (green arrow), blurry bacterial membranes (purple arrow), leaked intracellular substrates (light purple arrow) can be found in FM + NIR group. It stemmed from the local hyperthermia and produced ROS, which disturbed bacterial membrane permeability and damaged the phospholipid bilayers of the bacterial membrane, conclusively leading to bacterial matrix leakage.^[32] The leaked protein and ONPG content of *S. aureus* in the supernatant were further explored (Figure 4F). The significantly elevated

absorbance can be detected under NIR irradiation, especially for the groups of FeMoS₄ + NIR and FM + NIR.

Biofilms represent surface-adhered microbial communities embedded within a self-secreted extracellular polymeric matrix, exhibiting significantly enhanced resistance compared to planktonic bacteria.^[33] To address this challenge, we systematically evaluated the anti-biofilm efficacy of the synthesized materials. Crystal violet staining assays (Figure 4G,H) revealed markedly reduced purple coloration in MXene + NIR, FeMoS₄ + NIR, and FM + NIR groups, with FM demonstrating the most pronounced biofilm inhibition. Quantitative analysis corroborated this visual observation, showing a reduction in biofilm biomass for FM + NIR compared to untreated controls. These results fully prove that the FM BioHJzyme provides sufficient inhibitory ability against pathogenic bacteria including both Gram-positive and Gram-negative bacteria as well as their biofilms.

To elucidate the antibacterial mechanism of FM + NIR, we conducted transcriptomic profiling of *S. aureus* using RNA-seq technology. Principal component analysis (PCA) revealed distinct clustering patterns between PBS-treated and FM-treated groups (Figure 5A), establishing a statistically valid foundation for subsequent differential expression analysis. Comparative transcriptomic analysis demonstrated significant gene expression alterations, with volcano plot visualization identifying 323 up-regulated and 46 down-regulated differentially expressed genes (DEGs) in the FM group compared to PBS controls (Figure 5B). The main genes were marked by different color, which indicated the genes were enriched in metabolic pathway. Hierarchical clustering analysis of DEGs shown in the heating mapping (Figure 5C) confirmed pronounced transcriptional divergence between the groups. Gene Ontology (GO) enrichment analysis (Figure 5D) revealed significant modulation of biological processes and molecular functions, with particular emphasis on metabolic pathway regulation. Kyoto Encyclopedia of Genes and Genomes (KEGG) pathway analysis (Figure 5E) identified differential pathway activation patterns: up-regulated pathways were predominantly associated with metabolic processes (including selenocompound metabolism, purine metabolism, and thiamine metabolism), cellular processes (biofilm formation), and environmental information processing (phosphotransferase system), while down-regulated pathways primarily involved organismal systems (notably the NOD-like receptor signaling pathway). Further pathway annotation (Figure 5F) highlighted significant enrichment in ko01100 (Carbohydrate metabolism), particularly glycolysis/gluconeogenesis.^[34] These collective findings demonstrate that FM-mediated ROS generation exerts significant inhibitory effects on critical metabolic pathways in *S. aureus*, providing mechanistic insights into its growth-suppressive activity.

Subsequently, the biocompatibility profile and therapeutic efficacy were systematically evaluated through in vitro cytocompatibility assays and in vivo infectious wound models. Mouse fibroblast L929 cell line was selected to assess the biocompatibility of samples. The SEM and CLSM images of cells on Day 1 (Figure 6A) revealed preserved cellular integrity, with cells cultured on material surfaces demonstrating normal adhesion and spreading morphology. Cell counting kit-8 (CCK-8) results of cells with/without NIR irradiation on Day 1, 3, and 5 (Figure 6B) presented that the cell proliferated with the increased time, in which the cells of MXene group grew comparatively slower. A

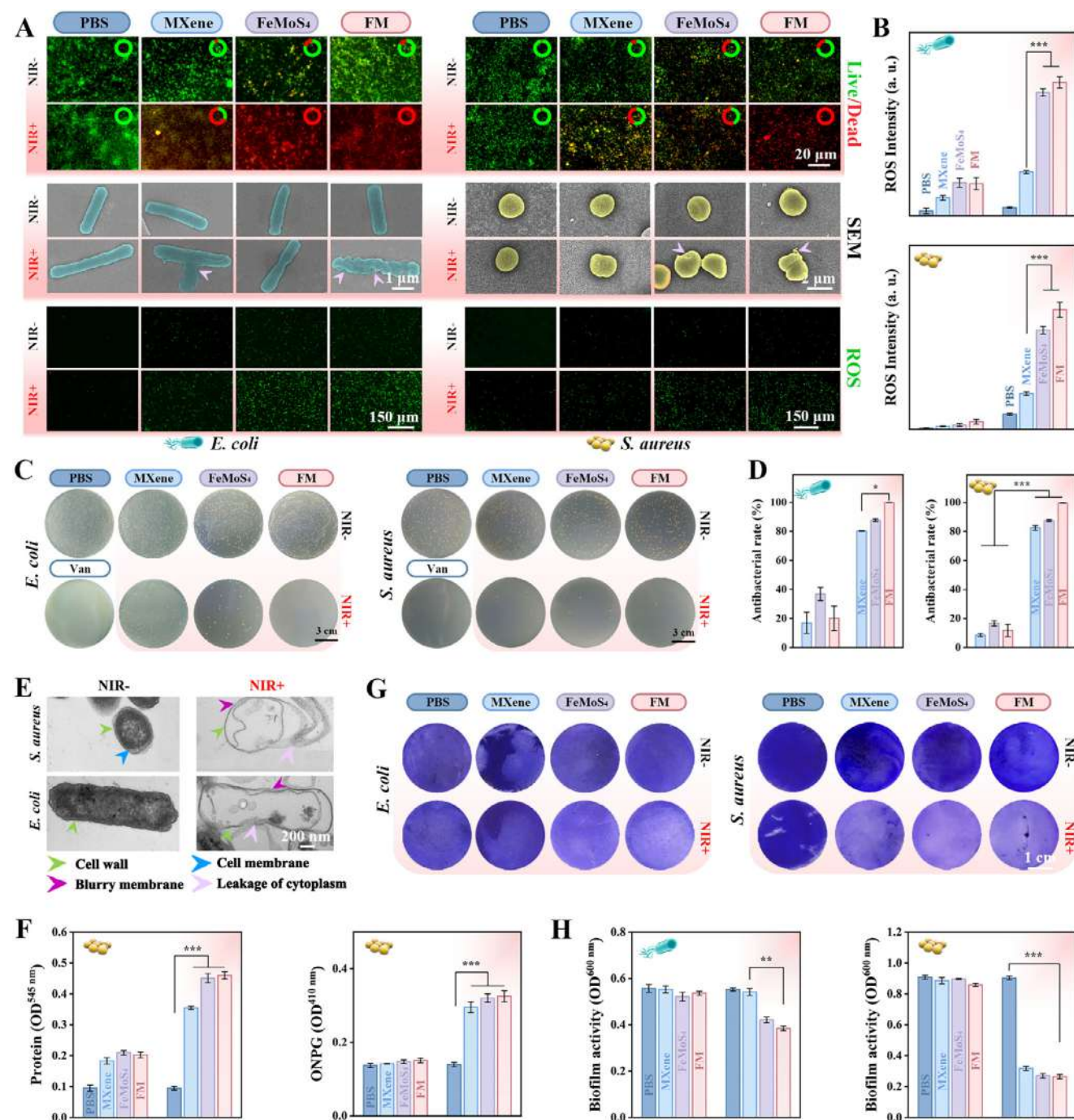


Figure 4. In vitro antibacterial capabilities. A) Live/Dead staining, SEM images and florescent ROS stained by DCFH-DA of *E. coli* and *S. aureus*; B) The quantitative analysis of ROS intensity; C) Spread plate results of *E. coli* and *S. aureus* with different samples and D) the corresponding antibacterial efficiency; E) Bacterial TEM images of FM group with/without NIR irradiation; F) The protein and ONPG content of *S. aureus* leaked in the supernatant after different treatments with/without NIR irradiation; G) Graphs of crystal violet staining of biofilms and H) its quantitative analysis. ($n = 5$; $*p < 0.05$, $**p < 0.01$, $***p < 0.001$).

standardized scratch assay was conducted to evaluate cell migration capacity (Figure 6C). The FeMoS₄ and MXene groups exhibited preferable cell migration compared with the others, revealing the potential wound healing promotion in vivo. The above results indicated that the added FeMoS₄ enhanced the biocompatibility

of MXene, while the FM possessed the strongest antibacterial capability.

The rat animal models with infectious wound were established and used to evaluated the antibacterial and wound healing capabilities in vivo. The Vancomycin (Van) drug was set as a positive

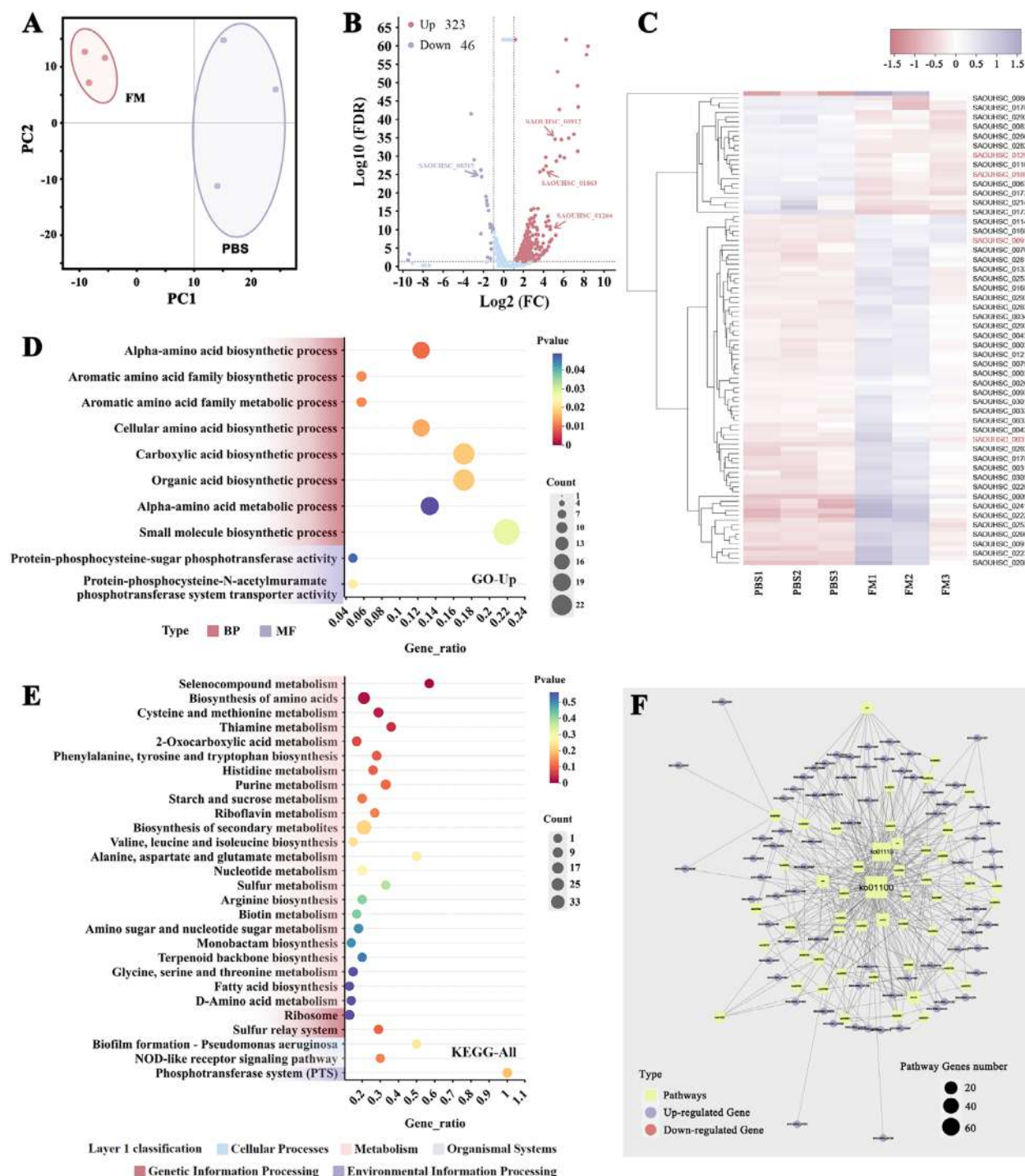


Figure 5. RNA-seq of *S. aureus* in comparison of PBS and FM + NIR. A) PCA analysis; B) Volcano plot; C) GO enrichment analysis; D) Heat mapping comparing PBS and FM; E) KEGG enrichment analysis; F) Differentially expressed gene KEGG annotation.

control. The photos of wound healing process (Figure 6D) with the increased time showed a decreased tendency, in which the FM + NIR group has a similar wound closure with Van group. The bacteria in the wound were obtained and cultured on AGAR medium as shown in Figure 6E. The number of bacterial colonies obviously reduced for the groups of FM and FM + NIR, indi-

cating the favorable antibacterial capability, which is conducive to the wound healing. The wound closure was further quantitatively analyzed (Figure 6F). It can be found that the NIR irradiation can accelerate wound healing owing to the superior bacterial killing, while the FM + NIR group had 88.66% wound closure at day 7% vs 53.51% in PBS control. In the therapeutic process,

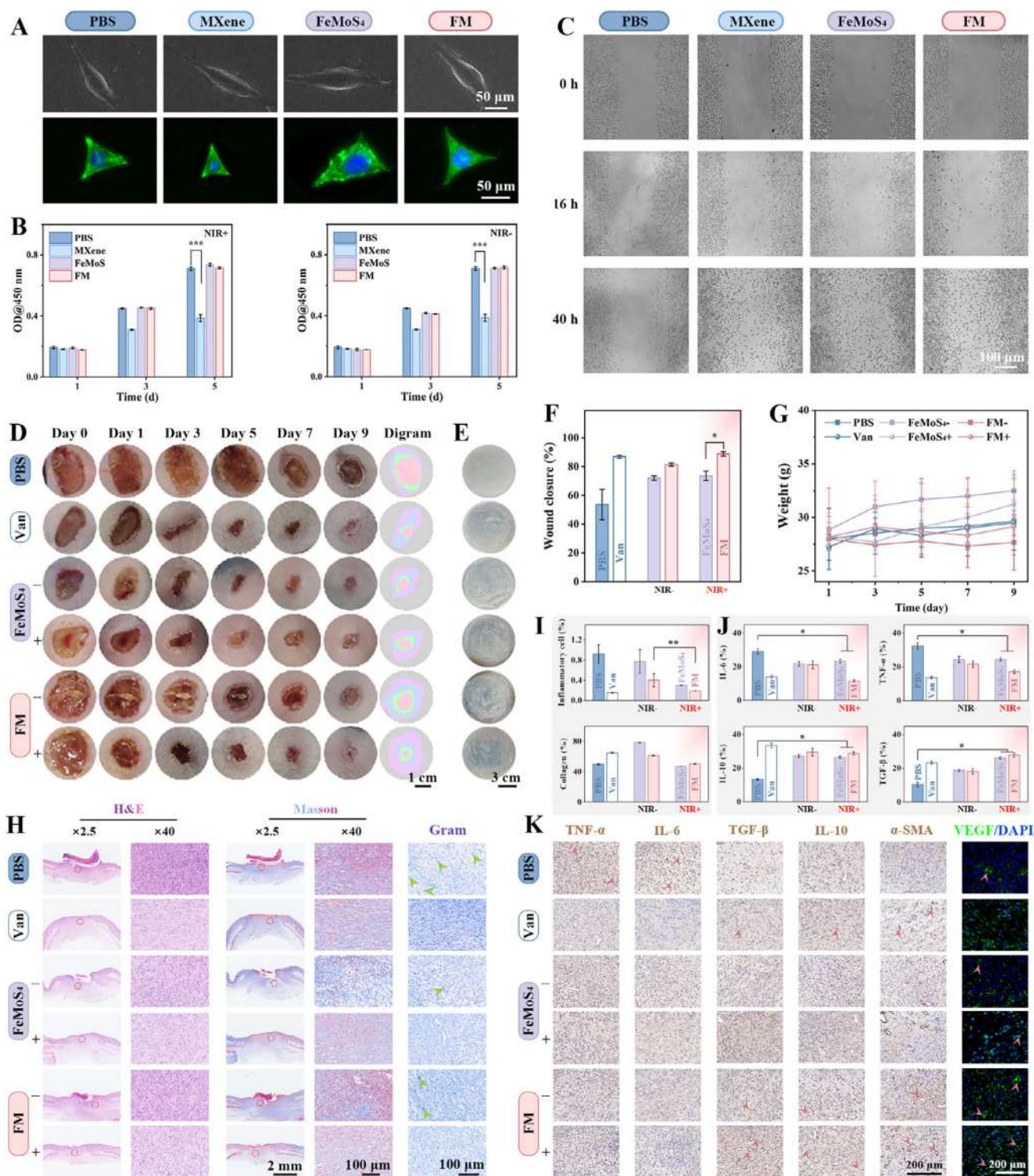


Figure 6. Biocompatibility and in vivo infectious wound healing. A) SEM and CLSM images of L929 cells on Day 1; B) CCK-8 results of cells co-cultured with samples with/without NIR irradiation; C) Scratch assay images of L929 cells; D) The wound images and the schematically visual illustration with the increased time; E) Spread plate images cultured by the bacteria on the wound; F) Quantitative analysis of wound closure; G) The weight change of the mice; H) The H&E, Masson and Gram staining and I) the corresponding quantitative analysis of H&E and Masson staining for inflammatory cells and collagen formation; J, K) TNF- α , IL-6, TGF- β , IL-10, α -SMA and VEGF staining as well as the corresponding quantitative analysis of TNF- α , IL-10, TGF- β , and IL-10 (pink arrows indicate the positive area). ($n = 5$; * $p < 0.05$, ** $p < 0.01$, *** $p < 0.001$).

the mice weight maintained stable, indicating the health state (Figure 6G).

After treatment, the wound skin of the mice was obtained, fixed, and first stained by hematoxylin and eosin (H&E), Masson, and Gram staining (Figure 6H). From the H&E staining, there were no obvious scab for the Van, FeMoS₄ + NIR, and FM + NIR groups, suggesting preferable skin repair. Masson staining can reflect the collagen deposition. The bluer staining, the more deposited collagen. The statistical analysis of H&E staining represents the inflammatory cell number, while the quantitative analysis of Masson staining reflects the percentage of collagen deposition (Figure 6I). Gram staining confirms the FM + NIR group exhibited minimum amount of bacterial residue, in which the green arrow represented bacteria. Subsequently, the immunohistochemical staining was processed. M1 related markers, such as Tumor Necrosis Factor- α (TNF- α) and Interleukin-6 (IL-6), and M2 related markers, including Transforming Growth Factor beta (TGF- β) and Interleukin-10 (IL-10) as well as the markers associated with angiogenesis (α -Smooth Muscle Actin (α -SMA) Vascular Endothelial Growth Factor (VEGF)) were stained to indicate the pro-inflammatory property, anti-inflammatory property and angiogenesis promotion of the samples (Figure 6K). The brown staining indicates the positive area. The significantly down-regulated TNF- α and IL-6 can be detected in the FM + NIR group, while the anti-inflammatory cytokine TGF- β and IL-10 was overexpressed in the FM + NIR group. The quantitative analysis of TNF- α , IL-6, TGF- β , and IL-10 was also shown in Figure 6J. The results implied that the FM can accelerate epithelialization, enhance collagen deposition, and angiogenesis to promote infectious wound healing, which was comparable to Van antibiotics without developing drug resistance.

The pro-inflammatory and anti-inflammatory mechanism was explored by RNA-seq through co-culturing with mouse mononuclear macrophage leukemia cells (RAW264.7).^[35] According to the PCA analysis (Figure 7A), the PBS and FM groups exhibit significant difference, which is valid for further analysis. Figure 7B showed the volcano graph of PBS and FM. The obvious up- and down-regulated DEGs were found with number of 26 and 1352, respectively. The top 5 genes were marked, which were Ass1, Bmpr2, Ap5m1, Apbb3, and Bclaf3, respectively. The heat mapping (Figure 7C) largely confirmed the distinct genetic differences between the groups. According to GO enrichment analysis (Figure 7D), all terms (biological process, cellular component, and molecular function) were regulated. The up-regulated GO analysis focused on the metabolic process and protein binding, while the down-regulated GO analysis referred to cellular metabolic process, membrane-bounded organelle, and DNA binding. KEGG enrichment analysis (Figure 7E) noted that the up-regulated pathways pointed to the Genetic information process (including Ribosome), Environmental information process (such as DNA-sensing pathway, Chemokine signaling pathway, and NOD-like receptor pathway etc.), and Metabolism (Biosynthesis of arginine, amino acids, et al.). The down-regulated pathways enriched at genetic information process (including Spliceosome, Protein processing in endoplasmic transport), Environmental information process (such as ECM-receptor interaction, TNF signaling pathway, etc.), and Organismal systems (Circadian rhythm, NOD-like receptor signaling pathway, and Dopaminergic synapse etc.). Additionally, the genes enriched by GO

were analyzed by protein-protein interaction (PPI) as shown in Figure 7F, indicating a strong expression relationship between them. Figure 7G illustrates the selectively splicing event types, including the retained intron (RI), mutually exclusive exons (MXE), alternative 5' splice site (A5SS), alternative 3' splice site (A3SS), and skipped exon (SE) to compare FM and PBS groups. The results verified the obvious modulation at the genetic level.

Furthermore, the samples used for in vivo treatments inevitably contact with blood, therefore, the hemocompatibility of the samples also needs to be carefully evaluated. The hemocompatibility were evaluated by the hemolysis assay and coagulation tests. The hemolysis results (Figure S11, Supporting Information) show that all samples expect for DI water group maintained at a normal level with the hemolysis rate less than 5%. In addition, the coagulation indicators, including activated partial thromboplastin time (APTT), prothrombin time (PT), thrombin time (TT), and fibrinogen (FIB) are in a normal state (Figure S12, Supporting Information). These results show that the samples have favorable hemocompatibility without hemolysis and coagulation. The main organs of mice (spleen, lung, heart, liver, and kidney) were performed to H&E staining, as seen in Figure S15 (Supporting Information), the samples have no obvious negative effect on all organs, demonstrating the biological safety of the samples.

The additional application forms of FM BioHJzyme with excellent antibacterial and wound healing capabilities were explored through the *in-situ* fabrication of FM/bacterial cellulose (FM/BC) wound dressing. The BC as extracellular polysaccharide is produced in the metabolic process of acetobacter xylinum. The FM/BC wound dressing can be prepared by co-culturing the FM and acetobacter xylinum. The SEM images and EDS mapping (Figure 8A) showed that the pure BC exhibited a fiber reticular structure, while the FM/BC demonstrated the FM nested in the fibrous network. XPS was applied to detect the chemical states, which reflected a similar conclusion with the above-mentioned XPS analysis of FM. The water absorption of FM/BC (Figure 8D) showed that the wound dressing can absorb PBS solution with a percentage of 94.41% \pm 4.96 %. More important, in vivo wound healing of PBS, BC-, BC+, FeMoS₄ + BC- (Fe/BC-), Fe/BC+, FM/BC-, and FM/BC+ groups were applied. The staining of IL-6, IL-10, VEGF, and Gram and its corresponding quantitative analysis were shown in Figure 8E,F. The FM BioHJzyme in a form of wound dressing can maintain superior anti-inflammatory property and angiogenic property and anti-bacterial property. The results verify that the FM BioHJzyme can be applied in diversified forms.

3. Conclusion

Collectively, FeMoS₄/MXene BioHJzyme exhibited robust enzyme-mimetic properties to improve ROS yield. Under NIR irradiation, the electron-hole separation occurred between MXene and FeMoS₄ owing to the heterostructure. Furthermore, in the phase of FeMoS₄, the added Mo pushed adjacent reactants (H₂O₂, H₂O, and O₂) closer to Fe by electronic push-pull effect, making the feedstocks more likely to capture electrons. Additionally, the decreased d-band center owing to the added Mo weakened the adsorption energy of intermediates enhancing the ROS production, resulting in the excellent antibacterial

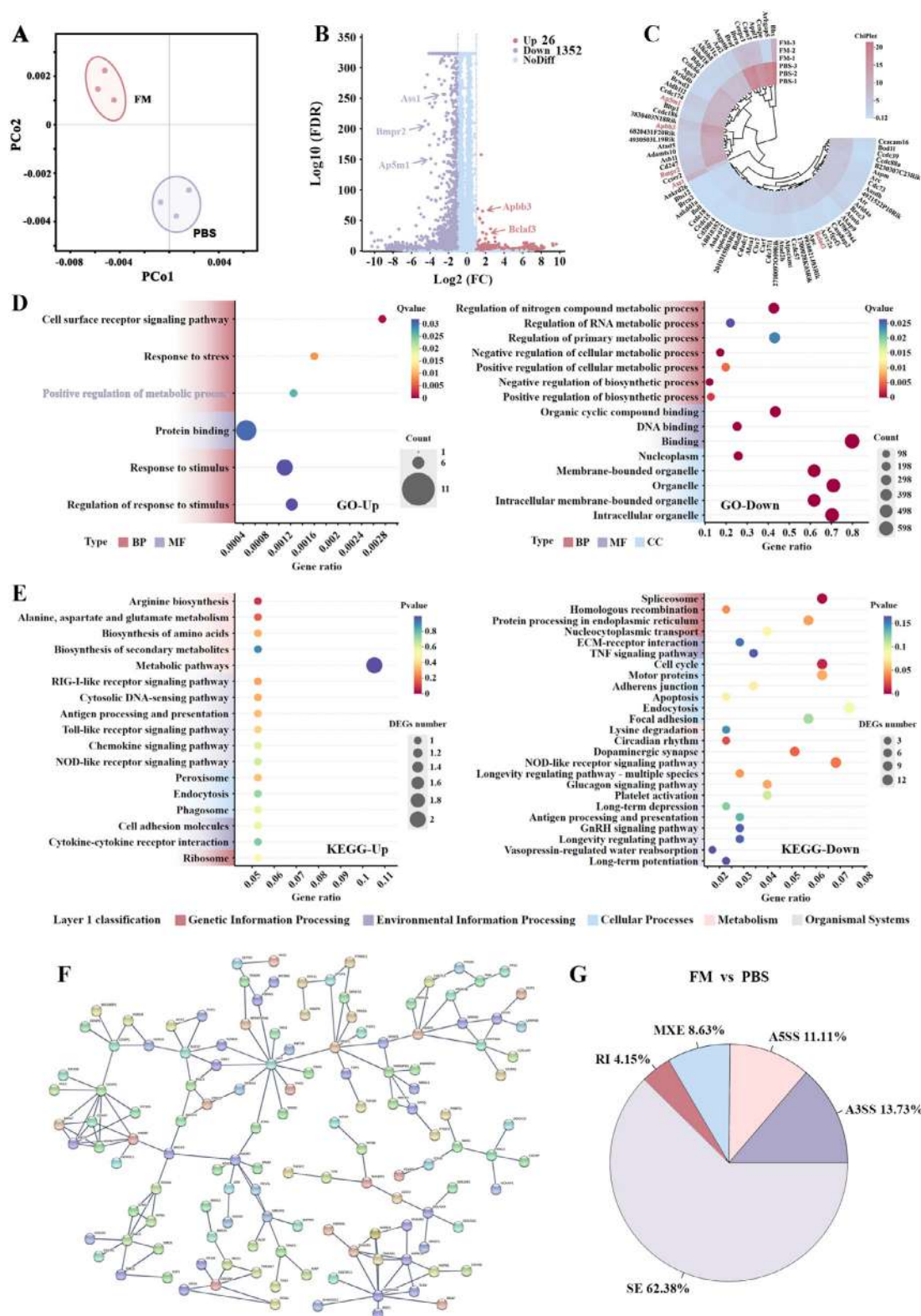


Figure 7. RNA-seq of RAW 264.7 cells in comparison of PBS and FM. A) PCA analysis; B) Volcano plot; C) Heat mapping comparing PBS and FM; D) The up-regulated and down-regulated GO enrichment; E) The up-regulated and down-regulated KEGG enrichment analysis; F) The PPI network diagram; G) AlterSplice of FM vs PBS.

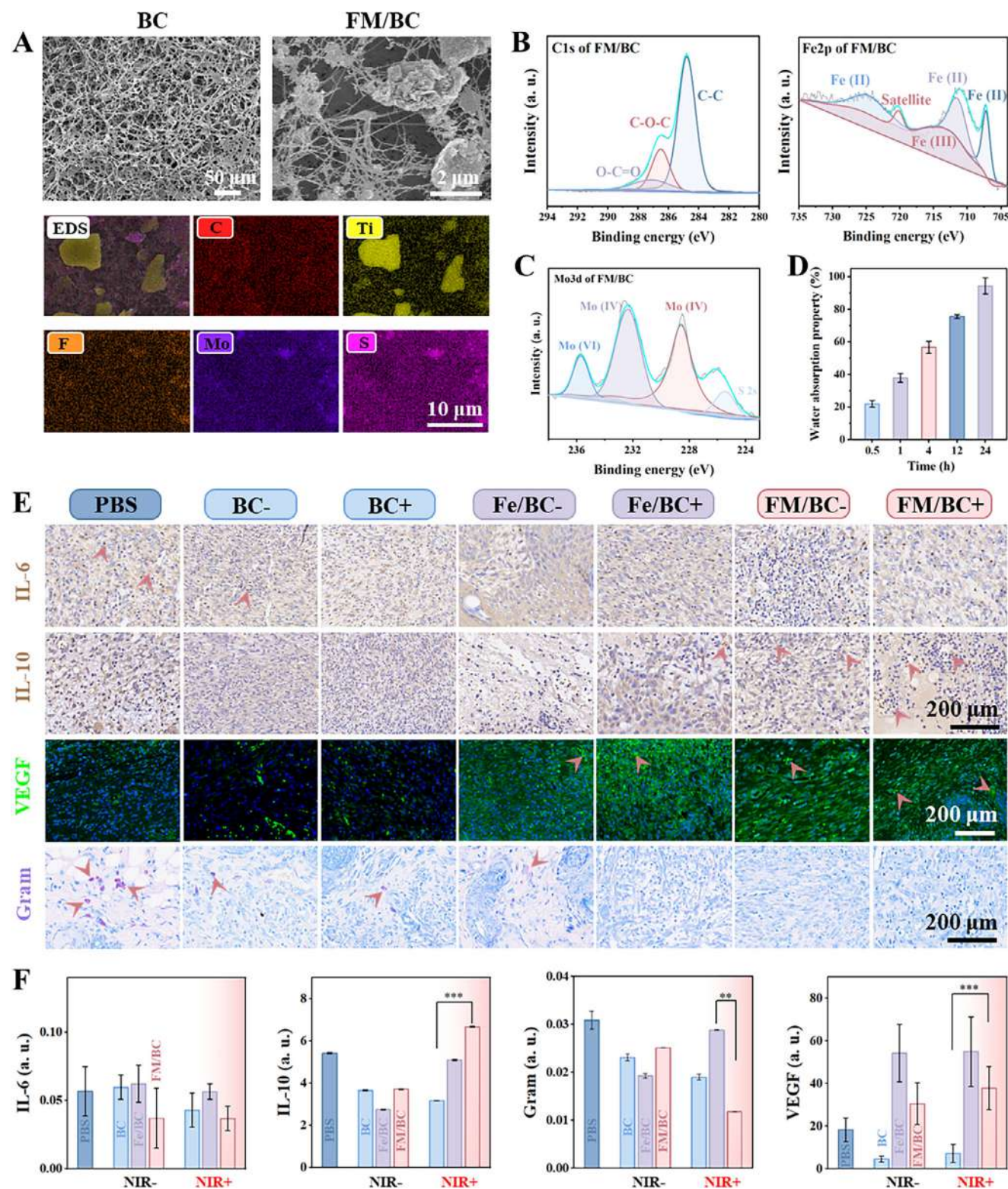


Figure 8. The application of FM in the formation of wound dressing by integrating with bacterial cellulose. A) SEM images of BC and FM/BC; B) The C 1s and Fe 2p deconvolution of FM/BC in XPS analysis; C) The Mo 3d deconvolution of FM/BC in XPS analysis; D) Water absorption property of FM/BC; E) IL-6, IL-10, VEGF, and Gram staining of different samples and F) the corresponding quantitative analysis. ($n = 5$; $*p < 0.05$, $**p < 0.01$, $***p < 0.001$).

efficiency. Followed, in the absence of NIR irradiation, the FM showed favorable anti-inflammatory and angiogenic property. This work enhanced the understanding of the intricate catalytic antibacterial mechanism in the BioHJzyme platform, verified the mechanism-performance relationship, and provided a mechanism-guided materials design. The FM can also be applied as a formation of wound dressing presenting the same remediation effect, providing a transformative strategy for developing adaptive wound management systems.

4. Experimental Section

Synthesis of FeMoS_4 and FM BioHJzyme: Single-layered MXene was prepared via ultrasonic stripping method.^[21] For FM synthesis, 400 mg ammonium tetrathiolobylate ($(\text{NH}_4)_2\text{MoS}_4$) was dispersed in deionized (DI) water, followed by addition of 140 mg iron oxyhydroxide (FeOOH). Subsequently, 200 mg MXene was introduced into the mixed solution and sonicated for 20 min. The dispersion was hydrothermally treated at 160 °C for 10 min in a sealed reactor. The resulting product was centrifuged at 8000 rpm for 10 min, with the supernatant discarded and the precipitate collected as FM BioHJzyme. The FeMoS_4 control group was synthesized through an identical procedure excluding MXene addition.

Synthesis of BC, Fe-BC, and FM-BC: Bacterial cellulose (BC) membranes were biosynthesized using acetobacter xylinum (ATCC 23767) cultured in yeast-glucose-chloramphenicol (YGC) agar medium. The medium was refreshed every 48 h for 14 days. Harvested BC films were purified by boiling in 2.5% NaOH solution at 80 °C for 3–4 h, followed by five DI water rinses under boiling conditions. For Fe-BC fabrication, FeMoS_4 nanoparticles ($200 \mu\text{g mL}^{-1}$) were incorporated into the YGC medium during bacterial culture. FM-BC was prepared analogously using FM BioHJzyme instead of FeMoS_4 .

Material Characterization: Morphological features were analyzed by scanning electron microscopy (SEM, JSM-7600F, JEOL, Japan) and transmission electron microscopy (TEM, SHZ-D, JEOL, Japan) with energy-dispersive X-ray spectroscopy (EDS). Crystalline structures were determined via X-ray diffraction (XRD, Empyrean, Panalytical, Netherlands). Chemical bonding states were characterized by X-ray photoelectron spectroscopy (XPS, Kratos AXIS Ultra, Shimadzu, Japan) and Fourier-transform infrared spectroscopy (FTIR, Nicolet IS20, Thermo Scientific). Surface charge properties were evaluated using a Zetasizer Nano-ZS-90 (Malvern). Reactive oxygen species (ROS) generation under irradiation was monitored by electron spin resonance spectroscopy (ESR, JES-FA200, JEOL) and UV-vis spectroscopy (U-3010, Hitachi, Japan). Photoelectrochemical properties were assessed via I-t curves recorded on a workstation (CH Instruments) using a standard three-electrode system (Ag/AgCl reference, Pt counter). Elemental release was quantified by inductively coupled plasma optical emission spectroscopy (ICP-OES, Thermo).

Photothermal Capability: An 808 nm NIR laser ($0.5\text{--}2 \text{ W cm}^{-2}$) coupled with an FLIR E6 thermal imager monitored temperature profiles. Samples ($50, 100, 200 \mu\text{g mL}^{-1}$) were irradiated at varied power densities ($0.5, 1.0, 1.5 \text{ W cm}^{-2}$) for 10 min. Cyclic stability tests comprised three heating-cooling cycles (10 min irradiation at 1.5 W cm^{-2} followed by 10 min natural cooling).

NIR-Induced ROS Production: POD-mimetic activity, which generate $\bullet\text{OH}$, was assessed through methylene blue (MB) and rhodamine B (RhB) degradation under NIR-II irradiation (1.5 W cm^{-2}). Reaction mixtures containing sample ($400 \mu\text{L}$, 1 mg mL^{-1}), H_2O_2 ($100 \mu\text{L}$, 30%), and dye ($400 \mu\text{L}$, 80 mg mL^{-1}) were equilibrated in darkness for 30 min prior to irradiation. After NIR-II irradiation (1.5 W cm^{-2}) for 10 min, UV-vis absorption spectra ($550\text{--}750 \text{ nm}$) were recorded using a spectrophotometer.^[36] 3,3',5,5'-tetramethylbenzidine (TMB, Aladdin) was also used to explore the POD-mimetic activity of different samples. TMB solution ($400 \mu\text{L}$, 0.2 v) was mixed with H_2O_2 ($100 \mu\text{L}$, 30 %) in acetate buffer ($300 \mu\text{L}$), and then the sample ($200 \mu\text{L}$, 1 mm) were added to the above mixture. Additionally, TMB was applied to calculate the Michaelis constant (K_m). The reaction mixture was prepared in 100 mM sodium acetate-acetic acid buffer (2 mL,

pH 4.0) containing 1 mL of sample solution (0.1 mv), $40 \mu\text{L}$ of 10 mg mL^{-1} TMB substrate, and $50 \mu\text{L}$ of $1 \text{ M H}_2\text{O}_2$. The catalytic oxidation process was monitored by recording the time-dependent absorbance changes by UV-vis spectroscopy. Catalytic efficiency was determined through Michaelis-Menten steady-state analysis to quantify the catalytic efficiency of the system. K_m can be calculated based on the Michaelis-Menten Equation.^[37] Singlet oxygen ($^1\text{O}_2$) was detected via 1,3-diphenylisobenzofuran (DPBF) trapping ($600 \mu\text{L}$ ethanol solution), with absorbance measured at 410 nm. $600 \mu\text{L}$ sample (1 mm) was dispersed in $600 \mu\text{L}$ DPBF (in ethanol) solution and incubated for 30 min. After NIR-II irradiation (10 min, 1.5 W cm^{-2}), the optical density (OD) value of the supernatant was measured using an ultraviolet spectrophotometer (UV-1800PC, AOELAB, China).^[18b]

GPx-Mimetic Activity: As an important antioxidant in bacteria, GSH can prevent the damage of reactive oxygen species to bacteria. GSH consumption capacity of the samples was evaluated using Ellman's reagent-based colorimetric assay. The experimental setup comprised: 0.5 mm carbonate-buffered saline (CBS, pH 9.6), 0.8 mm GSH solution, 5 mm Tris-HCl buffer (pH 8.0), and 10 mm DTNBS. H_2O_2 (1 mm) served as positive control, and PBS (pH 7.4) was as negative control. Following sample-GSH mixture preparation, experimental groups underwent 10 min NIR irradiation (808 nm , 1.5 W cm^{-2}) while non-irradiated controls were maintained in light-proof conditions at 37 °C for 15 min. Post-reaction supernatants obtained by centrifugation. The recorded optical density (OD) values were used to calculate GSH depletion efficiency according to the standard formula.^[38]

In vitro Antibacterial Assays: *S. aureus* and *E. coli* were exploited as representatives of typical Gram-positive and Gram-negative bacteria models.^[25] Spread plate method, SEM, TEM, Live/Dead staining, crystal violet staining, bacterial membrane permeability assay and ROS level in bacteria were detected, respectively to investigate the antibacterial effect. Quantitatively, the spread plate method was employed to measure the antibacterial efficiency in accordance of our lab's protocol. Specifically, the samples (0.2 mg mL^{-1}) were mixed with bacterial suspension ($600 \mu\text{L}$, $1 \times 10^5 \text{ CFU mL}^{-1}$), which were irradiated by 10 min 1.0 W cm^{-2} NIR laser and in dark as control. The mixture was evenly spread on Luria Bertani (LB) agar and cultured at 37 °C for 24 h. The colony units (CFU) was counted, and the antibacterial efficiency was calculated.^[4]

SEM and Live/Dead BacLight bacterial viability Kit (Solarbio, China) was applied for evaluating the antibacterial ability of the samples. The bacterial suspension ($600 \mu\text{L}$, $1 \times 10^8 \text{ CFU mL}^{-1}$) was incubated in 48-well plates for 12 h and then treated by different samples with/without NIR for 10 min. The bacteria were then stained with a Live & Dead BacLight bacterial viability kit for 15 min and detected by Inverted fluorescence microscope (CKX53, OLYMPUS, Japan).

In vitro anti-biofilm activity was evaluated through crystal violet staining. The bacterial fluid ($1 \times 10^8 \text{ CFU mL}^{-1}$, $600 \mu\text{L}$) was continuously cultured in 48-well plates containing cell slide for 5 days to form biofilms. The media were replaced every 24 h and washed with sterile PBS. After treated with different samples (1 mm , $200 \mu\text{L}$) + $1 \mu\text{g mL}^{-1}$ lactic acid under 1.5 W cm^{-2} NIR for 10 min, the cell slide with biofilm was fixed with 2.5 % glutaraldehyde for 20 min and dyed by 0.5 % crystal violet. The stained biofilm was imaged using a scanner (Epson Perfection V19). The ROS level in bacteria was detected by ROS assay kit (Solarbio, Beijing, China). 1 mL bacterial suspension was cultured in a 48-well plate for 12 h, which was illuminated by 1.5 W cm^{-2} NIR-II laser for 10 min after treated with 1 mg mL^{-1} different samples + $1 \mu\text{g mL}^{-1}$ lactic acid. The other samples were placed in the darkness for 10 min. After sucking out the supernatant, $200 \mu\text{L}$ dyeing working solution was added to the plate and incubated with different samples for 30 min. Fluorescent images were taken using an inverted fluorescence microscope (CKX53).

Evaluation of Hemolysis and Cytocompatibility: Hemocompatibility assessment was conducted through a standardized hemolysis assay. Fresh ovine whole blood was subjected to 50-fold dilution using phosphate-buffered saline (PBS, pH 7.4). Test samples were subsequently introduced into the diluted blood suspension, with deionized water and PBS serving as positive and negative controls, respectively. All experimental groups underwent controlled incubation at 37 °C for 3 h in a thermostatic water bath. Following incubation, centrifugation was performed at 3500 rpm for

5 min (4°C) to separate erythrocyte debris. The hemoglobin release in supernatants was quantified by measuring optical density at 545 nm using a UV-vis spectrophotometer. Hemolysis percentage can be calculated. CCK-8 (Solarbio, Beijing, China) was selected to detect the biocompatibility of samples on day 1, 3, and 5, while cell morphology was recorded by SEM and Live/Dead staining (Solarbio, Beijing, China).

RNA-Seq Analysis: The samples were co-cultured with L929 cells overnight, the cells were digested and centrifuged (3000 rpm, 5 min), the supernatant was aspirated, and quickly stored in liquid nitrogen for further transcriptome analysis. Shanghai BIOZERON Biotechnology Co., Ltd accomplished total RNA extraction, RNA sequencing, and bioinformatic analysis.

Animal Experiments: All animal procedures were approved by the Animal Care and Use Committee of West China Hospital, Sichuan University (No. 2022045A). A full-thickness circular wound (8 mm diameter) was excised. Bacterial inoculation was performed by applying 20 µL of *S. aureus* suspension to the wound bed. After 24 h post-infection, 50 µL of sample solution (200 mg L⁻¹) was topically administered. The treatment group underwent 10 min irradiation with an 808 nm NIR laser, while real-time thermal imaging was captured using an infrared camera (FLIR E8, ±0.1°C resolution). Post-treatment, peri-wound exudates were collected via sterile swabs, serially diluted in sterile PBS, and inoculated onto LB agar plates using the spread plate technique. At day 7 post-treatment, mice were euthanized for tissue harvest. Wound beds and major organs (spleen, liver, heart, lungs, and kidneys) were fixed in 4% paraformaldehyde for 48 h. Tissue were subjected to H&E staining, immunofluorescence staining, and immunohistochemical staining. The main organs were stained by H&E staining.

Statistical Analysis: Three copies of the afore-mentioned tests were made. The mean value and standard deviation were used to display all experimental statistics. Based on a one-way analysis and the student's *t*-test, significant differences were determined using GraphPad Prism 8.0. In the current investigation, a value of **p* < 0.05 and ***p* < 0.01 was deemed statistically significant.

Supporting Information

Supporting Information is available from the Wiley Online Library or from the author.

Acknowledgements

This work is jointly funded by the National Natural Science Foundation of China (52302351, 32271392), National Key Research and Development Program of China (2022YFC2405703), Natural Science Foundation of Sichuan (2024NSFSC1239, 2024NSFSC0217, 2024NSFSC0676), China Postdoctoral Science Foundation under Grant Number 2023M732477 and 2024T170615, Chengdu Science and Technology Bureau Fund (2024-YF05-00026-SN, 2022-YF05-00094-SN). The authors thank Hui Wang, Jing Zhou, Xi Wu and Shuguang Yan (Analytical & Testing Center, Sichuan University) for their help in SEM, CLSM, ICP and XPS characterizations. The authors also would like to thank Yanping Huang from Center of Engineering Experimental Teaching, School of Chemical Engineering, Sichuan University for the help of SEM measurement. The authors thank Shanghai Daisuan Technology (www.daisuan.com) for the help in DFT simulations. The authors would like to thank Dong Yu with Digital scanning system (WISLEAP WS-10), Linzhu Li with Digital scanning system (Olympus VS200) and Lelica DMI 8 fluorescence microscope in Life Science Core Facilities (College of Life Sciences, Sichuan University). The authors extend their gratitude to Shiyanjia Lab (www.shiyanjia.com) for providing invaluable assistance with the SEM and TEM. The authors would like to thank Ceshigo Research Service (www.ceshigou.com) for providing ESR testing. Thanks to eceshi (www.eceshi.com) for PL analysis.

Conflict of Interest

The authors declare no conflict of interest.

Data Availability Statement

The data that support the findings of this study are available from the corresponding author upon reasonable request.

Keywords

antibacterial, electronic effects, enzyme, heterostructure, wound healing

Received: May 29, 2025

Revised: July 4, 2025

Published online:

- [1] A. Fleming, *Br. Med. J.* **1941**, 2, 386.
- [2] A. Bharadwaj, A. Rastogi, S. Pandey, S. Gupta, J. S. Sohal, *Biomed Res. Int.* **2022**, 2022, 5419874.
- [3] B. P. Lazzaro, M. Zasloff, J. Rolff, *Science* **2020**, 368, aau5480.
- [4] M. He, Y. Hou, Y. Jiang, Y. Li, Q. Zou, C. Chen, L. Zhang, W. Yang, *Mater. Lett.* **2019**, 235, 242.
- [5] A. Desireddy, B. E. Conn, J. Guo, B. Yoon, R. N. Barnett, B. M. Monahan, K. Kirschbaum, W. P. Griffith, R. L. Whetten, U. Landman, T. P. Bigioni, *Nature* **2013**, 501, 399.
- [6] F. Y. Rezaei, G. Pircheraghi, V. S. Nikbin, *ACS Appl. Nano Mater.* **2024**, 7, 15242.
- [7] a) Z. Ma, M. Yuan, Z. Cheng, Z. Yang, L. Yang, B. Liu, Y. Bian, A. A. Al Kheraif, P. a. Ma, J. Lin, *Chem. Eng. J.* **2024**, 482, 148711; b) K. Chae, W. Y. Jang, K. Park, J. Lee, H. Kim, K. Lee, C. K. Lee, Y. Lee, S. H. Lee, J. Seo, *Sci. Adv.* **2023**, 6, abb0025.
- [8] H. Fei, J. Dong, Y. Feng, C. S. Allen, C. Wan, B. Voloskiy, M. Li, Z. Zhao, Y. Wang, H. Sun, P. An, W. Chen, Z. Guo, C. Lee, D. Chen, I. Shakir, M. Liu, T. Hu, Y. Li, A. I. Kirkland, X. Duan, Y. Huang, *Nat. Catal.* **2018**, 1, 63.
- [9] a) D. G. Franchina, H. Kurniawan, M. Grusdat, C. Binsfeld, L. Guerra, L. Bonetti, L. Soriano-Baguet, A. Ewen, T. Kobayashi, S. Farinelle, A. R. Minafra, N. Vandamme, A. Carpentier, F. K. Borgmann, C. Jäger, Y. Chen, M. Kleinewietfeld, V. Vasilou, M. Mittelbronn, K. Hiller, P. A. Lang, D. Brenner, *Nat. Commun.* **2022**, 13, 1789; b) J. Huo, Q. Jia, H. Huang, J. Zhang, P. Li, X. Dong, W. Huang, *Chem. Soc. Rev.* **2021**, 50, 8762.
- [10] O. Akhavan, E. Ghaderi, *ACS Nano* **2010**, 4, 5731.
- [11] a) T. Dutta, R. Sarkar, B. Pakhira, S. Ghosh, R. Sarkar, A. Barui, S. Sarkar, *RSC Adv.* **2015**, 5, 80192; b) V. Lakshmi Prasanna, R. Vijayaraghavan, *Langmuir* **2015**, 31, 9155.
- [12] O. Akhavan, E. Ghaderi, A. Esfandiar, *J. Phys. Chem. B* **2011**, 115, 6279.
- [13] S. Liu, T. H. Zeng, M. Hofmann, E. Burcombe, J. Wei, R. Jiang, J. Kong, Y. Chen, *ACS Nano* **2011**, 5, 6971.
- [14] A. Kumar, A. K. Pandey, S. S. Singh, R. Shanker, A. Dhawan, *Free Radical Biol. Med.* **2011**, 51, 1872.
- [15] M.-Y. Wu, L. Chen, Q. Chen, R. Hu, X. Xu, Y. Wang, J. Li, S. Feng, C. Dong, X.-L. Zhang, Z. Li, L. Wang, S. Chen, M. Gu, *Adv. Mater.* **2023**, 35, 2208578.
- [16] L. Wang, C. Hu, L. Shao, *Int. J. Nanomed.* **2017**, 12, 1227.
- [17] Y. Zhu, W. Wang, J. Cheng, Y. Qu, Y. Dai, M. Liu, J. Yu, C. Wang, H. Wang, S. Wang, C. Zhao, Y. Wu, Y. Liu, *Angew. Chem., Int. Ed.* **2021**, 60, 9480.
- [18] a) M. He, Z. Wang, D. Sun, Y. Deng, W. Yang, G. Yin, *Adv. Funct. Mater.* **2025**, 35, 2421228; b) M. He, Z. Wang, D. Xiang, D. Sun, Y. K. Chan, H. Ren, Z. Lin, G. Yin, Y. Deng, W. Yang, *Adv. Mater.* **2024**, 36, 2405659.
- [19] M. He, Z. Wang, H. Yang, Q. Wang, D. Xiang, X. Pang, Y. K. Chan, D. Sun, G. Yin, W. Yang, Y. Deng, *Adv. Sci.* **2023**, 10, 2300986.

- [20] Y. Deng, X. Lian, Z. Lin, D. Sun, H. Zou, Y. K. Chan, W. Yang, M. He, G. Yin, *Adv. Funct. Mater.* **2025**, 35, 2414823.
- [21] X. Gao, M. He, W. Chen, Z. Wang, Y. Li, D. Bai, G. Yin, R. Shu, Y. Deng, W. Yang, *Adv. Funct. Mater.* **2024**, 34, 2408236.
- [22] P. Morozzi, B. Ballarin, S. Arcozzi, E. Brattich, F. Lucarelli, S. Nava, P. J. Gómez-Cascales, J. A. G. Orza, L. Tositti, *Atmos. Environ.* **2021**, 252, 118297.
- [23] H. Jin, T. Zhu, X. Huang, M. Sun, H. Li, X. Zhu, M. Liu, Y. Xie, W. Huang, D. Yan, *Biomaterials* **2019**, 211, 68.
- [24] M. Li, L. Li, K. Su, X. Liu, T. Zhang, Y. Liang, D. Jing, X. Yang, D. Zheng, Z. Cui, Z. Li, S. Zhu, K. W. K. Yeung, Y. Zheng, X. Wang, S. Wu, *Adv. Sci.* **2019**, 6, 1900599.
- [25] X. Zhou, Z. Wang, Y. K. Chan, Y. Yang, Z. Jiao, L. Li, J. Li, K. Liang, Y. Deng, *Adv. Funct. Mater.* **2022**, 32, 2109469.
- [26] H. Yu, H. Deng, J. He, J. D. Keasling, X. Luo, *Nat. Commun.* **2023**, 14, 8211.
- [27] Q. Jing, Z. Mei, X. Sheng, X. Zou, Q. Xu, L. Wang, H. Guo, *Adv. Funct. Mater.* **2024**, 34, 2307002.
- [28] C.-F. Li, L.-J. Xie, J.-W. Zhao, L.-F. Gu, H.-B. Tang, L. Zheng, G.-R. Li, *Angew. Chem., Int. Ed.* **2022**, 61, 202116934.
- [29] X. Liang, N. Fu, S. Yao, Z. Li, Y. Li, *J. Am. Chem. Soc.* **2022**, 144, 18155.
- [30] H. Fei, J. Dong, M. J. Arellano-Jiménez, G. Ye, N. Dong Kim, E. L. Samuel, Z. Peng, Z. Zhu, F. Qin, J. Bao, M. J. Yacaman, P. M. Ajayan, D. Chen, J. M. Tour, *Nat. Commun.* **2015**, 6, 8668.
- [31] Z. Shen, X. Jin, J. Tian, M. Li, Y. Yuan, S. Zhang, S. Fang, X. Fan, W. Xu, H. Lu, J. Lu, H. Zhang, *Nat. Catal.* **2022**, 5, 555.
- [32] M. He, X. Yang, D. Xiang, Y. K. Chan, G. Yin, W. Yang, Y. Deng, *Nano Lett.* **2025**, 25, 6828.
- [33] a) Y. Dergham, D. Le Coq, P. Nicolas, E. Bidnenko, S. Dérozier, M. Deforet, E. Huillet, P. Sanchez-Vizueté, J. Deschamps, K. Hamze, R. Briandet, *Nat. Commun.* **2023**, 14, 7546; b) J.-L. Wang, X. Pan, X. Li, K.-M. Liu, M. Yao, J.-Y. An, Y. Wan, X.-Q. Yu, S. Feng, M.-Y. Wu, *Adv. Mater.* **2025**, 37, 2411468.
- [34] K. G. Hicks, A. A. Cluntun, H. L. Schubert, S. R. Hackett, J. A. Berg, P. G. Leonard, M. A. Ajalla Aleixo, Y. Zhou, A. J. Bott, S. R. Salvatore, F. Chang, A. Blevins, P. Barta, S. Tilley, A. Leifer, A. Guzman, A. Arok, S. Fogarty, J. M. Winter, M. C. Nonato, F. L. Muller, J. E. Cox, J. Rutter, *Science* **2023**, 379, 996.
- [35] X. J. Mi, H. M. Le, S. Lee, H. R. Park, Y. J. Kim, *ACS Omega* **2022**, 7, 42723.
- [36] M. Magro, G. Sinigaglia, L. Nodari, J. Tucek, K. Polakova, Z. Marusak, S. Cardillo, G. Salviulo, U. Russo, R. Stevanato, R. Zboril, F. Vianello, *Acta Biomater.* **2012**, 8, 2068.
- [37] Y. Long, L. Li, T. Xu, X. Wu, Y. Gao, J. Huang, C. He, T. Ma, L. Ma, C. Cheng, C. Zhao, *Nat. Commun.* **2021**, 12, 6143.
- [38] Z. Wang, M. He, X. Pang, G. Yin, Y. Deng, W. Yang, *Chem. Eng. J.* **2024**, 488, 151005.